OPEN ACCESS
IOP Publishing
Superconductor Science and Technology
Supercond. Sci. Technol. **34** (2021) 105001 (15pp)
https://doi.org/10.1088/1361-6668/ac1c13

High-temperature superconducting screens for magnetic field-error cancellation in accelerator magnets

L Bortot[1,2,*], M Mentink[1], C Petrone[1], J Van Nugteren[1], G Deferne[1], T Koettig[1], G Kirby[1], M Pentella[1,3], J C Perez[1], F O Pincot[1], G De Rijk[1], S Russenschuck[1], A P Verweij[1] and S Schöps[2]

[1] CERN, Espl. des Particules 1, CH-1211 Geneva, Switzerland
[2] Technische Universität Darmstadt, Karolinenplatz 5, DE-64289 Darmstadt, Germany
[3] Department of Applied Science and Technology, Polytechnic of Turin, Turin, Italy

E-mail: lorenzo.bortot@cern.ch

Received 26 March 2021, revised 2 August 2021
Accepted for publication 10 August 2021
Published 24 August 2021

Abstract

Accelerators magnets must have minimal magnetic field imperfections to reduce particle-beam instabilities. In the case of coils made of high-temperature superconducting (HTS) tapes, the magnetization due to persistent currents adds an undesired field contribution, potentially degrading the magnetic field quality. In this paper we study the use of superconducting screens based on HTS tapes for reducing the magnetic field imperfections in accelerator magnets. The screens exploit the magnetization by persistent currents to cancel out the magnetic field error. The screens are aligned with the main field component, such that only the undesired field components are compensated. The screens are self-regulating, and do not require any externally applied source of energy. Measurements in liquid nitrogen at 77 K show for dipole-field configurations a significant reduction of the magnetic field error up to a factor of four. The residual error is explained via numerical simulations accounting for the geometric defects in the HTS screens, achieving satisfactory agreement with experimental results. Simulations show that if screens are increased in width and thickness, and operated at 4.5 K, field errors may be eliminated almost entirely for the typical excitation cycles of accelerator magnets.

Keywords: high-temperature superconductors, magnetic field quality, screening currents, persistent magnetization, superconducting magnetic screens, finite-element analysis, accelerator magnets

(Some figures may appear in colour only in the online journal)

* Author to whom any correspondence should be addressed.

1. Introduction

Future circular accelerators for high-energy particle physics are expected to rely on increasingly higher magnetic fields for steering and focusing the particle beams [1]. A promising strategy for producing high magnetic fields consists in adopting accelerator magnets based on high-temperature superconducting (HTS) tapes [2]. Such tapes are made of rare-earth cuprate compounds (ReBCOs) which have an estimated upper critical field of 140 T [3] and a critical temperature of 93 K. Consequently, HTS magnets are expected to be operated at fields beyond 20 T [2] and with enthalpy margins one order of magnitude above traditional low temperature superconducting (LTS) materials, such as Nb-Ti or Nb_3Sn [4].

Independently of the adopted technology, accelerator magnets must generate high-quality magnetic fields in their magnet aperture, with imperfections limited to a few units in 10^{-4} of the main magnetic field [5, 6], because field imperfections can lead to particle-beam instabilities [7]. The field quality is determined by magnet design features such as coil geometry and mechanical tolerances, and influenced by material properties such as saturation and hysteresis of the iron yoke. Moreover, time-transient effects such as mechanical deformation due to Lorentz forces, and magnetization due to eddy currents and screening currents in normal conducting and superconducting materials are expected to have detrimental effects.

Screening currents are particularly relevant in ReBCO tapes, since they behave in the same way as wide, anisotropic mono-filaments, resulting in persistent screening currents. The related magnetization adds an undesired contribution that detrimentally affects the magnetic field quality [8, 9] and decays with a time constant longer than the duty-cycle of the magnet. The degradation of the magnetic field is particularly pronounced at low currents, because the persistent magnetization current is only limited by the superconducting current density, which is the highest at lowest field.

Previous work for mitigating magnetic field imperfections led to magnetic cloaks for sensors [10, 11], shim coils for magnetic resonance imaging [12] and nuclear magnetic resonance [13] applications, and selective shields for field homogenization in solenoids [14]. Recently, persistent-current shims coils were proposed as a conceptual solution for improving the field quality in accelerator magnets [15, 16]. The coils are designed as magnet inserts, implementing a canted-cosine theta layout. Moving from this concept, we propose in this paper HTS screens based on superconducting tapes for the passive field-error cancellation in accelerator magnets.

We present a proof of concept using HTS screens in a dipole-field configuration. The screens exploit the magnetization produced by persistent currents to shape the magnetic field in the magnet aperture. The screens, made by stacks of tapes arranged in layers, are aligned with the main field component such that only the imperfections in the magnetic field are suppressed. The alignment is made possible thanks to the high aspect ratio between the width and thickness of the tapes. The screens are self-regulating, do not require active control, and store a negligible fraction of the total magnetic energy of the magnet as they do not form any closed loop. The proposed design is called HALO (Harmonics-Absorbing-Layered-Object) which is fully scalable and expandable.

The prototype consists in two HTS screens aligned in a parallel configuration (see figure 1). The screens are inserted in the aperture of a dipole magnet which magnetic field is perturbed by means of iron bars. Four iron configurations are investigated, differing in the field-error magnitude. The HTS screens are activated by cooling the prototype to 77 K with liquid nitrogen. The persistent magnetization due to screening current reduces the magnetic field error by a factor of three to four.

The prototype is simulated in the 2D setting using the finite element method, implementing a coupled $\boldsymbol{A}$-$\boldsymbol{H}$ field formulation [17–19] for HTS magnets [20]. The numerical model is used for evaluating the performance limits of the prototype, tracing the residual error measured in the magnetic field due to geometric defects, and simulating the HTS screens for working conditions typical of accelerator magnets.

The working principle of the HTS screen is discussed in section 2. The experimental setup is shown in section 3, followed by description of the mathematical model in section 4. Numerical and experimental results are given in section 5, extrapolated in section 6 and discussed in section 7. Conclusions are given in section 8.

2. Working principle

The working principle is discussed with regards to a non-magnetized shell with finite thickness δ_s and constant resistivity ρ. The cross section of the shell is shown in figure 2(a), together with a local coordinate system $(\parallel, \perp)$ oriented accordingly to the shell wide surface. The shell is exposed to an externally applied magnetic flux density $\boldsymbol{B}_s(\boldsymbol{r}, t)$ depending on space $\boldsymbol{r} \in \mathbb{R}^3$ and time $t \in \mathbb{R}$, with initial condition $\boldsymbol{B}_s(\boldsymbol{r}, 0) = 0$. All the magnetic properties are considered as constant. Starting from Faraday's law, the screening current density $\boldsymbol{J}_i$ induced in the shell is obtained as

$$\nabla \times \rho \boldsymbol{J}_i + \partial_t(\boldsymbol{B}_s + \boldsymbol{B}_i) = 0, \tag{1}$$

where $\boldsymbol{E} = \rho \boldsymbol{J}_i$ denotes the electric field driving the screening currents, and $\boldsymbol{B}_i$ is the magnetic contribution from the shell to the magnetic flux density $\boldsymbol{B} = \boldsymbol{B}_s + \boldsymbol{B}_i$. The distribution of the magnetic flux lines is shown in figure 2(b).

By assuming negligible thickness for the shell, that is, $\delta_s \to 0$ (see figure 2(c)), the magnetic coupling occurs only for the normal component of the external field source, leaving the parallel component unaffected. At the same time, the induced current density flows only in the plane of the shell. Then, the differential operators and vectors $\boldsymbol{v}$ are decomposed into their tangential and normal components (superscripts $\parallel$ and $\perp$), that is, $\nabla = \nabla^{\parallel} + \nabla^{\perp}$ and $\boldsymbol{v} = \boldsymbol{v}^{\parallel} + \boldsymbol{v}^{\perp}$, accordingly to the local coordinate system in figure 2(a). With these definitions, (1) is reduced to

$$\nabla^{\perp} \times \rho \boldsymbol{J}_i^{\parallel} + \partial_t(\boldsymbol{B}_s^{\perp} + \boldsymbol{B}_i^{\perp}) = 0. \tag{2}$$

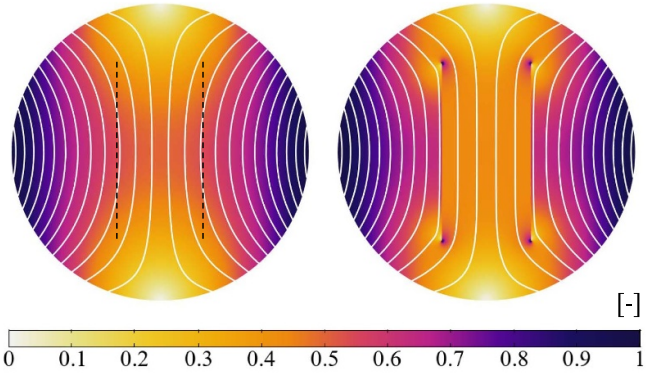

Figure 1. Example showing a normalized, non-ideal dipole magnetic field, before (left) and after (right) the introduction of the HTS screens. The expected and actual position of the screens is marked by dashed and solid lines.

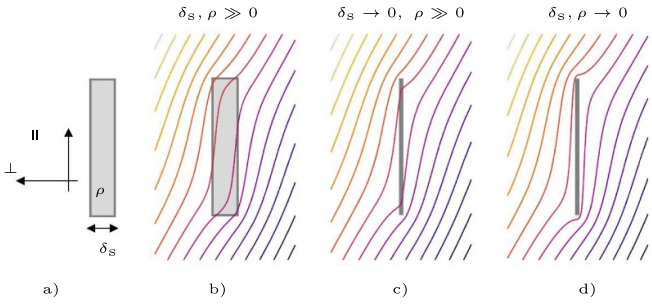

Figure 2. (a) Cross-section of a non-magnetized, conducting shell of thickness δ_s and resistivity ρ. The magnetic flux lines distribution is shown for the cases of (b) finite δ_s and ρ, (c) negligible δ_s but finite ρ, and (d) negligible δ_s and ρ.

By assuming negligible resistivity for the shell, $\rho \to 0$ (see figure 2(d)), the material becomes a perfect electrical conductor (PEC). As a consequence, (2) is reduced to

$$\partial_t(\boldsymbol{B}_s^{\perp} + \boldsymbol{B}_i^{\perp}) = 0, \tag{3}$$

showing that the magnetic field has a constant value within the shell. Since the external field was initially zero, $\boldsymbol{B}_i^{\perp}$ is always equal and opposite to $\boldsymbol{B}_s^{\perp}$. The screening currents are persistent, exhibiting no decay time, and their magnitude is determined by the magnetization required to completely cancel out the externally applied field. PECs are therefore ideal magnetic screens.

Although perfect electrical conductors are a mathematical abstraction, the superconducting properties of the tapes provide a reasonable approximation of $\rho \to 0$, allowing for persistent magnetization generated by screening currents. This phenomenon is combined together with the strong geometric anisotropy of the tapes and their negligible thickness, creating a selective magnetic coupling with respect to the spatial components of the applied field. By choosing a suitable orientation, the tapes can be used to guide the magnetic field, achieving a field correction only for specific field components. This is obtained by aligning the tapes with the main field direction, such that the cancellation effect occurs only for the undesired field components. The tapes can be arranged side by side into layers, increasing the equivalent screening surface. Layers can be stacked on top of each other to increase the magnetic screening properties. The working principle is shown by the example in figure 1, where a non-ideal dipole magnetic field is shown before (left) and after (right) the introduction of the HTS screens.

The working principle is applicable also to 2D magnetic field configurations with higher number of magnetic poles (for example quadrupole fields) as long as the superconducting screens are shaped accordingly to the main field component.

3. Experimental setup

The proof of concept aims at demonstrating that the magnetic field quality can be improved in a given region of space by means of persistent screening currents. The proof is achieved by using differential measurements, that is, by assessing the magnetic field quality with and without the presence of the HTS screens.

Four key-elements are included in the experimental setup: (a) a dipole field of known magnetic properties, provided by the reference dipole MCB24 from the Magnetic Measurement laboratory at CERN; (b) a source of field perturbation, that is, two iron bars introduced in the magnet aperture; (c) the field-error cancellation source, provided by means of two HTS screens; (d) a magnetic measurement system for characterizing the field quality, composed of a rotating coil [21, 22], a motor drive, and the data acquisition system for processing the probe signal. The experimental setup is detailed in the remainder of the section.

3.1. Prototypes

The mechanical assembly is composed of an aluminum base plate, a stainless steel tube, two bars made of iron and a box made of polymide foam, hosting the HTS holder with the superconducting screens. The assembly is shown in figures 3 and 4 (left).

The plate provides both the mechanical reference for the alignment in the magnet aperture and the mechanical support for the remaining parts. The tube protecting the field measurement system is bolted by means of collars to the front and back folded tabs of the plate. The iron bars are bolted on perforated folded tabs located on the left and right sides of the plate. A set of holes allows the iron bars to be vertically displaced, in order to investigate the field-error cancellation for different field-error scenarios.

The box is leak-tight and works as a cryostat for the cool down of the HTS screens to 77 K in a bath of liquid nitrogen. The box is machined such that a central groove on the bottom ensures the clearance for the tube containing the rotating coil, whereas two lateral grooves on the top allow the HTS-screen holder to slide into the box. The HTS holder provides the mechanical support for keeping the screens in parallel position. For this setup, two prototype iterations for the HTS holder were developed and tested.

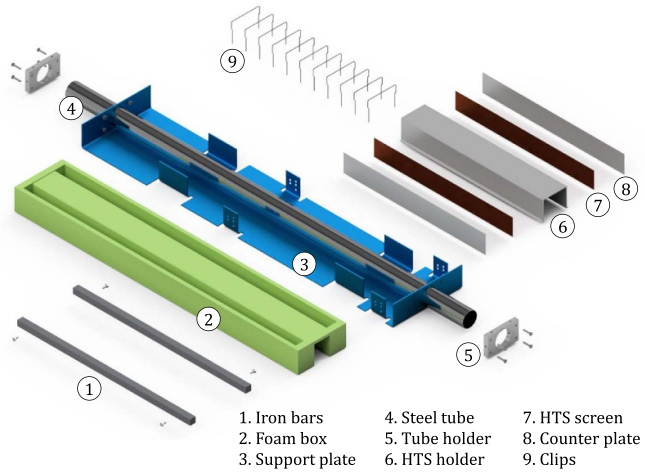

Figure 3. Exploded view of the parts of the experimental assembly. (1) Iron bars, (2) polymide foam box, (3) aluminum support plate, (4) stainless steel tube, (5) aluminum collars, (6) aluminum HTS holder, (7) HTS screens, (8) aluminum counter plates, (9) stainless steel clips.

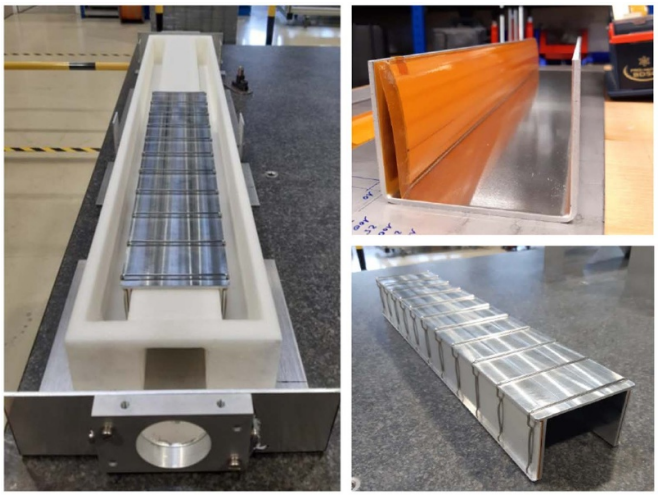

Figure 4. Left: experimental assembly. The support plate at the bottom bottom holds the iron bars, the foam box and the stainless steel tube which is blocked by means of two supports at the plate ends. The holder is settled inside the foam box. Right, top: first HTS holder prototype, obtained by bending an aluminum plate and fixing the screen using adhesive tape. Right, bottom: second HTS holder prototype, obtained by machining an aluminum block and fixing the tapes using aluminum counter-plates and clips.

The HTS screens are made of commercially available, second-generation HTS tapes; their relevant parameters are given in table 1. The HTS spool is cut in 500 mm long tapes which are arranged in a multi-layered composite structure, as shown in figure 5, left. Each layer is obtained by attaching the tapes to a 25 μm thick layer of epoxy adhesive, and then the layers are stacked on top of each other.

An offset equal to half of the tape width is introduced between each layer, leading to a brick wall structure. The offset

Table 1. Tape specifications (self field).

Parameter	Unit	Value	Description
Superpower [23]			Producer
SCS12050-AP			Tape label
Hastelloy C-276			Substrate
δ_w	mm	12	Tape width
δ_t	μm	100	Tape thickness
$\delta_{t,Sc}$	μm	1	ReBCO thickness
$\delta_{t,Ag}$	μm	2	Silver thickness
$\delta_{t,Cu}$	μm	20	Copper thickness
$\delta_{t,Hs}$	μm	50	Hastelloy thickness
n-value	—	28	Power-law index
$I_{c,min}$ (77 K)	A	304	Minimum critical current
$I_{c,avg}$ (77 K)	A	320	Average critical current
σ_{I_c}	—	0.042	Standard deviation

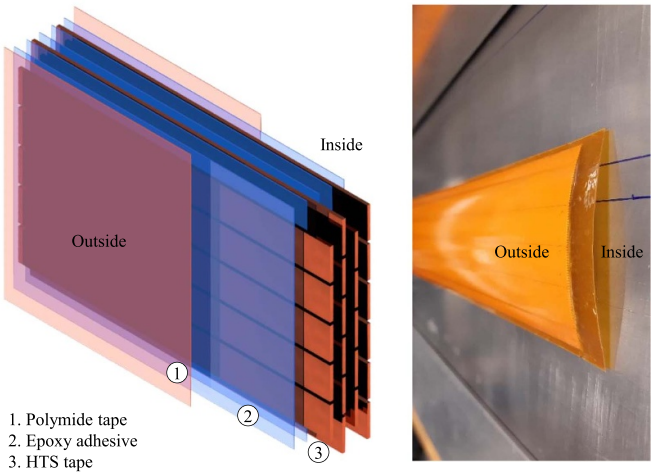

Figure 5. Left: multi-layered composite structure characterizing the HTS screens. Four layers of HTS tapes are arranged in a stack by means of adhesive tape which provides also electrical insulation. Right: one of the two HTS screens used for the proof of concept.

improves the screening properties of the structure by preventing the magnetic flux lines to penetrate in the gaps between the tapes. For symmetry reasons, the even-order layers are one tape-width less wide than the odd-order layers. The screens are sealed with 75 μm thick polymide foils, applied on each side. Such structure is mechanically flexible and scalable for both the screen width and thickness, ensuring electrical insulation between each HTS layer and for the overall screen.

Two four-layer, 60 mm wide screens are manufactured for the proof of concept, with the layers containing five and four tapes. The maximum width of the screens is limited by the available space within the aperture of the reference magnet. One of the screens is shown in figure 5, right. The screen curvature is a consequence of stacking all the tapes on the same side, causing an amplification of the typical tape convexity. This behavior is not an issue as the screens are flexible enough to be straightened by the HTS holder. The curvature may be mitigated by flipping upside-down the tapes in every second layer of each screen.

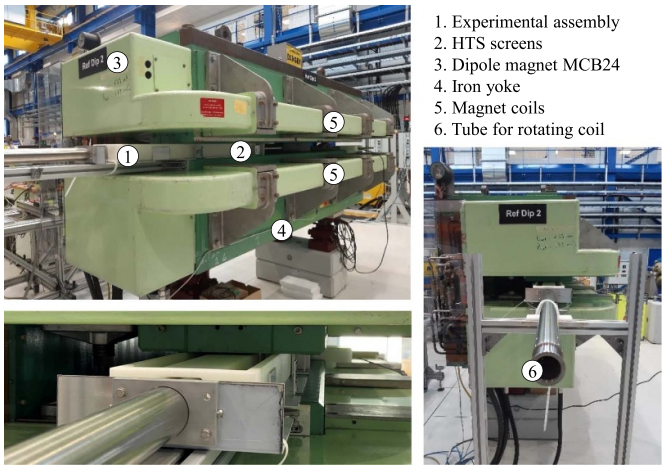

Figure 6. Top left: side view of the reference dipole magnet MCB24, with the setup mounted in the magnet aperture. Bottom left: detail of the magnet aperture. Right: front view of the magnet.

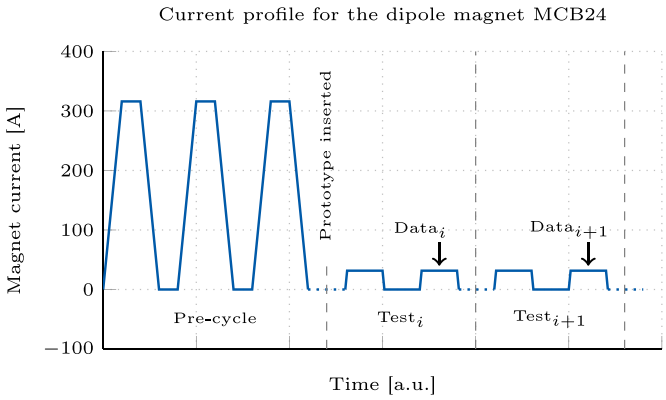

Figure 7. Current cycle used in the reference dipole magnet MCB24 for the experimental campaign.

The first prototype aimed for the simplicity of construction (see figure 4, top right). The holder was obtained by bending an aluminum plate, and is used to keep in place the screens by compressing them between the holder and the foam box. However, the mechanical alignment of the first prototype is not sufficiently accurate for the proof of concept. The experience gained from the first holder led to the improved design of the second prototype (see figure 4, bottom right). Here, two aluminum counter-plates provide a compression force to keep the screens straightened. The counter-plates are pushed by clips made of non-magnetic stainless steel, positioned at every 50 mm along the holder. With respect to the previous version, the second prototype is characterized by a smaller mechanical tolerance and higher stiffness, producing a better cancellation of the field error. For this reason, experimental activity focused mainly on the second prototype.

3.2. Dipole magnet

The reference dipole magnet used for the experiment is shown in figure 6. The magnet is normal conducting and has a linear transfer function of 316 $\mathrm{A\,T^{-1}}$ for the 0–1 T field range. The magnet is always operated after an initial de-gaussing cycle. Before each experiment, the magnet goes through a pre-cycle, such that the magnetization of the iron yoke is kept consistent through all the measurements. The profile used for the source current $i_\mathrm{m}(t)$ is shown in figure 7. The pre-cycle consists in a trapezoidal profile, going from zero up to the nominal current $I_\mathrm{n} = 316$ A, and back.

After the pre-cycle, the setup is fixed into the magnet aperture. As the foam box is designed 500 mm longer than the screen, it sticks out of the magnet aperture (see figure 6, bottom), leaving sufficient space for adding the coolant from outside the magnet coils. Each test cycle is composed by two consecutive trapezoidal curves, up to the peak current $I_\mathrm{p} = 31.6$ A, producing a magnetic field in the magnet aperture of 100 mT. The peak value of the magnetic field is kept low for both preventing the reduction of the critical current in the tapes, and limiting the magnetic forces on the iron bars. The current is kept constant for about 120 s, to settle any dynamic effects. The measurements in each cycle are acquired for both the current plateaus, showing negligible difference. The data presented in this work are always taken from the second curve, where the HTS tapes are already magnetized.

3.3. Measurement system

Rotating coils, also known as harmonic coils, are electromagnetic transducers for measuring the b_k and a_k field multipoles (see the appendix). The coil shaft is positioned parallel to the magnetic axis of the magnet, and rotated in the magnet aperture. The change of flux linkage Φ induces, by integral Faraday's law $U_\mathrm{m} = -\mathrm{d}_t\Phi$, a voltage signal U_m which is measured at the terminals of the coil. By integrating in time the voltage signal, the flux linkage is obtained and given as a function of the series expansion of the radial field [6].

The rotating coil used for the HALO characterization is composed of a printed-circuit board (PCB), (36.5 mm in length and 47 mm in width), aligned with the longitudinal center of the HTS screens. The PCB contains five coils mounted radially, with an active surface of 320 $\mathrm{cm^2}$. CERN proprietary digital cards [24] integrate the induced voltages in the coils rotating at a frequency of 1 Hz. Each measurement is given by the average of sixty rotations of the coils. The measurements deliver a typical precision of a magnetic-field harmonic of ± 0.05 units.

4. Mathematical model

The field problem is formulated by combining a domain decomposition strategy with a dedicated coupled field formulation derived from [20], using a thin-shell approximation for the HTS tapes [20, 26]. The computational domain containing the reference dipole magnet and the experimental setup is presented in figure 8. The magnetic field, given in tesla, in the cross section of the reference dipole magnet is shown on the top. A detailed view of the magnet aperture containing the experimental setup and the iron bars which introduce a field

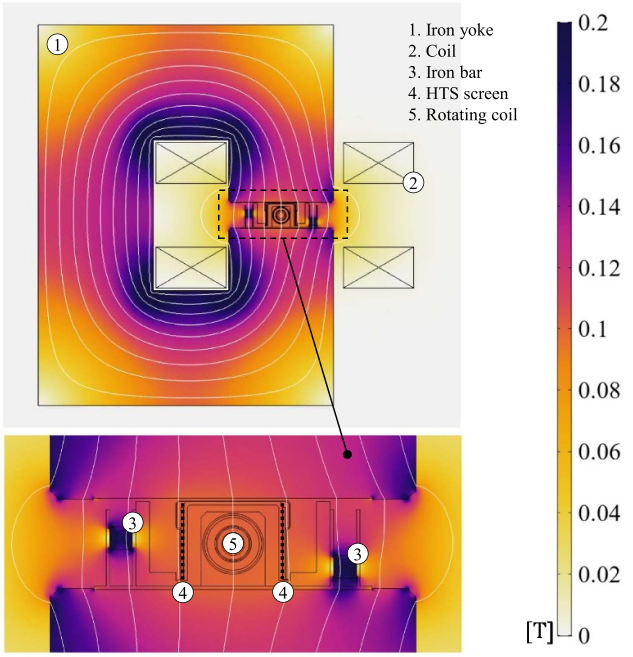

Figure 8. Top: magnetic field, in tesla, in the cross section of the reference dipole magnet. The field source is provided by means of a normal conducting coil, marked with crossed domains. The c-shaped iron yoke guides the field lines in the magnet aperture, where the experimental setup is positioned. Bottom: detail view of the magnet aperture containing the experimental setup and the iron bars which introduce a field perturbation. The position of the HTS screens is highlighted by dashed lines.

perturbation is given on the bottom. The position of the HTS screens is highlighted by dashed lines.

The field problem is solved under magnetoquasistatic assumptions for the magnetic field strength $\boldsymbol{H}$ [27, 28] in the superconducting tapes Γ_{H}^r, where $r = 1,\ldots,N_{\mathrm{t}}$ and N_{t} is the number of tapes, and for the reduced magnetic vector potential $\boldsymbol{A}^\star$ [29] in the region Ω_{A} representing the remaining of the model, that is, the normal conducting magnet and the air region. The formulation reads

$$\nabla \times \mu^{-1} \nabla \times \boldsymbol{A}^\star + \sigma \partial_t \boldsymbol{A}^\star - \boldsymbol{\chi}_{\mathrm{i}} i_{\mathrm{m}} = 0 \text{ in } \Omega_{\mathrm{A}}, \tag{4}$$

$$\nabla \times \rho \nabla \times \boldsymbol{H} + \partial_t \mu \boldsymbol{H} - \nabla \times \boldsymbol{\chi}_{\mathrm{u}}^r u_{\mathrm{s}}^r = 0 \text{ in } \Gamma_{\mathrm{H}}^r, \tag{5}$$

$$\delta_{\mathrm{t}} \int_{\Gamma_{\mathrm{H}}^r} \boldsymbol{\chi}_{\mathrm{u}}^r \cdot (\nabla \times \boldsymbol{H}) \, \mathrm{d}\Gamma = 0, \tag{6}$$

where σ and ρ are the electrical conductivity and resistivity, μ is the magnetic permeability, δ_{t} is the thickness of the tapes, i_{m} is the source current in the dipole magnet, u_{s}^r is the source voltage for the rth tape treated as an algebraic unknown. The winding functions $\boldsymbol{\chi}_{\mathrm{i}}$ and $\boldsymbol{\chi}_{\mathrm{u}}^r$ distribute the lumped source signals into the field model [30, 31]. The algebraic constraint (6) enforces a zero net current through each tape. The field formulation in (4)–(6) avoids the use of electrical conductivity for the superconducting domains ($\sigma \to \infty$) and the electrical resistivity for the non-conducting domains ($\rho \to \infty$), such that the material properties remain finite [19, 32].

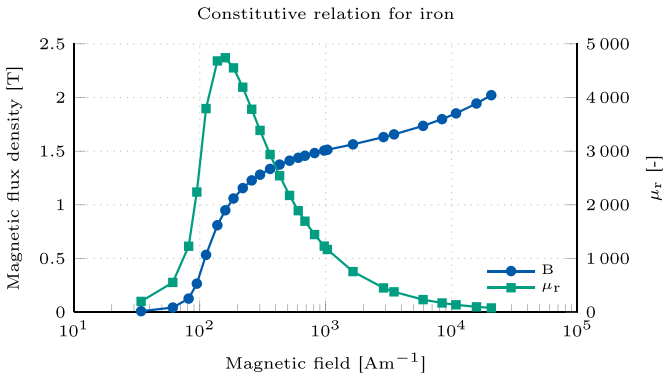

Figure 9. Measured B-H curve for the nonlinear $\mu(\boldsymbol{B})$ relation.

4.1. Constitutive relations

The ferromagnetic materials included in the model are made of pure iron (Fe $> 99.8\%$). The B-H relation was measured for a sample [33] and the resulting curve, displayed in figure 9, is used in the model for the $\mu(\boldsymbol{B})$ relation.

The highly nonlinear electric field-current density relation characterizing HTS materials (see e.g. [34]) is modeled by means of a power law [35]. Such simplified relation for the resistivity neglects frozen-field phenomena, occurring only in the low current density regime. The power law provides faster field relaxation and decay rates for screening-current phenomena with respect to the more complex percolation-depinning law [36, 37], therefore it is retained as conservative assumption. The resistivity is given by

$$\rho(|\boldsymbol{J}|, \boldsymbol{B}, T) = \frac{E_{\mathrm{c}}}{J_{\mathrm{c}}(\boldsymbol{B}, T)} \left(\frac{|\boldsymbol{J}|}{J_{\mathrm{c}}(\boldsymbol{B}, T)} \right)^{n(\boldsymbol{B},T)-1}, \tag{7}$$

where $\boldsymbol{J}$ is the current density, T is the temperature, E_{c} is the critical electric field set to 1×10^{-4} V m^{-1} [38], and the material- and field-dependent parameters J_{c} and n are the anisotropic critical current density and the power-law index, respectively. The power-law index was measured by the tape producer, and it is set to 28. The lifting function $f_{\mathrm{l}}(\boldsymbol{B}, T)$ implemented for J_{c} is shown in figure 10, for a background field of 100 mT. Data are taken from [25], where tapes from the same producer and technology were characterized. Then, J_{c} is obtained from $J_{\mathrm{c}} = f_{\mathrm{l}} I_{\mathrm{c,min}} / S_{\mathrm{Sc}}$ where the minimum critical current $I_{\mathrm{c,min}}$ and the superconductor cross section S_{Sc} are taken from table 1.

4.2. Geometric quality

A visual inspection of the experimental assembly highlighted gaps between the first prototype of the HTS holder and the foam box, as well as displacements and corrugations for both the left and right screens; see figure 11, left. Such undesired geometric defects arise from intrinsic stresses in the HTS tapes and were found to detrimentally affect the field quality.

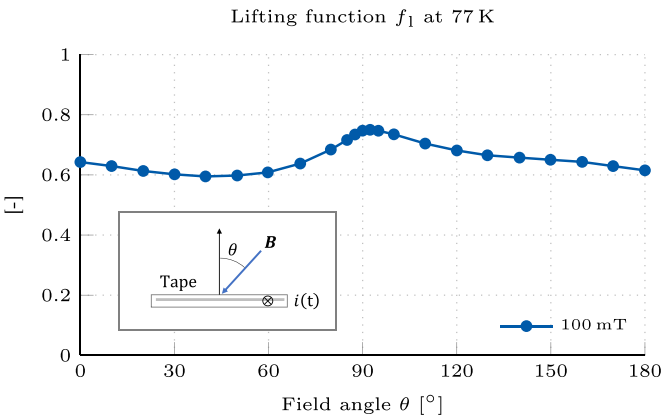

Figure 10. Lifting function as a function of the field angle, for tapes at 77 K and 100 mT, based on data from [25].

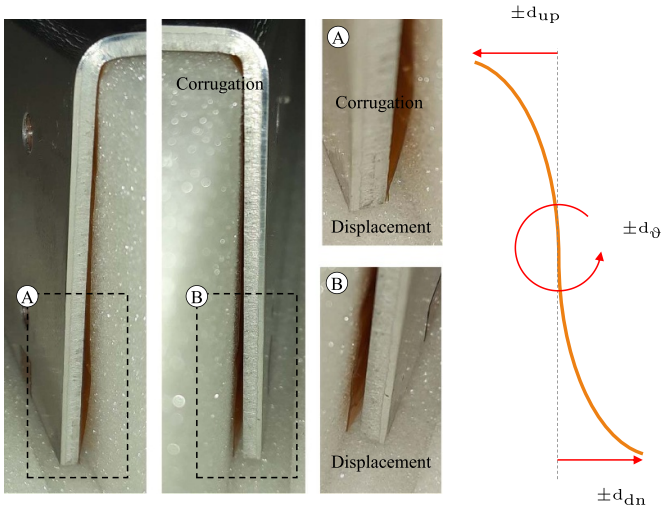

Figure 11. Left: visual inspection of the first HTS holder prototype, highlighting gaps between the holder and the foam box, as well as displacements and corrugations for both the left and right HTS screens. Right: geometric-defect parameters, used to implement a realistic geometry for the HTS screen.

The geometric defects introduced in the model are shown for one screen in figure 11, right. The HTS screens are implemented as two joint arcs of a parabola, whose shape is determined by the parameters d_{up} and d_{dn}. Screens are also allowed to rotate around their central point, accordingly to the angle d_θ. Three degrees of freedom are introduced for each screen, therefore the overall geometric defect $\mathbf{d}_g$ is defined for this model as

$$\mathbf{d}_g = \left[d^l_{up}, d^r_{up}, d^l_{dn}, d^r_{dn}, d^l_\theta, d^r_\theta\right]^\top, \tag{8}$$

with the superscripts l and r referring to the left and right screens. It is worth noting that flat screens are still possible with $d_{up}, d_{dn} \to 0$, whereas parallel screens require also $d_\theta \to 0$.

The MATLAB® [39] implementation of the particle swarm optimization (PSO) [40] is used to determine $\mathbf{d}_g$. The penalty function adopted for the PSO minimizes the difference between field quality measurements and simulations. The optimization problem reads

$$\begin{aligned} \min_{\mathbf{d}_g} \quad & \sum_{k=2}^{6} \left(|a^m_k - a^s_k(\mathbf{d}_g)| + |b^m_k - b^s_k(\mathbf{d}_g)|\right), \\ \text{s.t.} \quad & |d_{up}|, |d_{dn}| - x_{max} \leqslant 0, \\ & |d_\theta| - \theta_{max} \leqslant 0, \end{aligned} \tag{9}$$

with the coefficients a^m_k and b^m_k being derived from measurements, whereas $a^s_k(\mathbf{d}_g)$ and $b^s_k(\mathbf{d}_g)$ are calculated numerically. The maximum geometric errors in displacement and angle are set to $x_{max} = 2.5$ mm and $\theta_{max} = 50$ mrad. The index k is limited to the dodecapole component, given that high order field components are found to be of much lower magnitude. As discussed in section 5, the simulated field error arising from geometric defects is matched with the experimental observations.

5. Experimental and numerical results

The test campaign for the HALO experiments is organized in two parts, assessing the behavior of the HALO device without and with the iron bars.

In the first part, the HTS screens are characterized both at room temperature (300 K) and in liquid nitrogen (77 K), in a dipole background field. The first measurement determines the magnetic contribution from the normal conducting materials in the assembly. The second measurement quantifies the magnetic coupling of the HTS screens with the background field, which is strongly influenced by the precise alignment of the tapes with respect to the magnetic field lines. The two tests are carried out for both the prototypes of the HTS holder. Subsequently, these results are used for fitting the geometric-defect parameters and, therefore, calibrating the numerical model.

In the second part, iron bars are introduced in the magnet aperture, adding a field error to the dipole field of the reference magnet. The field error is modulated by applying to the left and right iron bars the vertical offsets Δy_l and Δy_r, in a range between $+5$ and -20 mm with respect to the horizontal mid-plane of the rotating coil. Four different scenarios are proposed. The first three scenarios feature an increasing magnitude for the field error, therefore they are labeled as *low*, *medium* and *high*. The fourth scenario is in an anti-symmetric configuration with respect to the second scenario, providing field errors of the same magnitude. It was used for checking the analysis method, therefore it is labeled as *check*. For each scenario, the field quality is measured first at 300 K, being affected only by the iron, and then at 77 K, where the HTS screens are also active. In this way, a comparison of the two measurements gives the net contribution of the HTS screens to the field-error cancellation.

The most relevant features for each of the tests are summarized in table 2. The first HTS holder prototype is characterized only for the *medium* error scenario, whereas the second prototype is characterized for all scenarios. All the test are performed in a background dipole field $B_{op} = 100$ mT, and the multipoles are evaluated at a reference radius $r_0 = 15$ mm.

Table 2. Test campaign.

No.	T_{op} (K)	Iron bars	Δy_l (mm)	Δy_r (mm)	Label
First HTS holder prototype					
1	300	No	n.a.		n.a.
2	77	No	n.a.		
3	300	Yes	+5	−20	Medium
4	77	Yes	+5	−20	
Second HTS holder prototype					
5	300	No	n.a.		n.a.
6	77	No	n.a.		
7	300	Yes	+5	+0	Low
8	77	Yes	+5	+0	
9	300	Yes	+5	−20	Medium
10	77	Yes	+5	−20	
11	300	Yes	−20	−10	High
12	77	Yes	−20	−10	
13	300	Yes	−20	+5	Check
14	77	Yes	−20	+5	

Note: $B_{op} = 100$ mT and $r_0 = 15$ mm for each test.

Measurements are compared with simulations. With respect to the tests at 77 K, two geometric models for each HTS screen prototype are considered. The first model assumes perfectly parallel and flat HTS tapes, whereas the second includes the geometric defects introduced in (8). All the simulations are carried out on a standard workstation (Intel® Core i7-3770 CPU @ 3.40 GHz, 32 GB of RAM, Windows-10® Enterprise 64-bit operating system), using the proprietary FEM solver COMSOL MULTIPHYSICS® [41].

5.1. Prototypes without iron bars

The magnetic field quality is evaluated with the experimental setup mounted without iron bars in the magnet aperture. Measurement and simulation results are given for the first prototype in figure 12(a). Measurements at 300 K quantify the influence of magnetization and dynamic phenomena possibly occurring in the experimental setup within 0.5 units of field error. Measurements with the HTS screen at 77 K show an undesired self-field error dominated by the a_2 and b_3 components, with contributions from b_2 and a_4. When corrected for geometric defects, both the measured and simulated THD factor for the first prototype is equal to 21. Note that for simulation without geometric defects, the calculated THD factor is almost zero, thus showing the importance of geometric defects on the overall result.

The same measurements and simulations are presented for the second prototype in figure 12(c). The field error at room temperature is unchanged, whereas measurements at cold show five units of a_2, with minor contributions below one unit, and a THD factor equal to 5. Therefore, the overall self-field error is reduced by about a factor of four compared to the first prototype. The simulations with geometric defects reproduce the measurement results quite well, which implies that the origin of the remaining field error is quite well understood, and further reductions of the THD factor seem quite feasible through improved manufacturing techniques.

The net magnetic contribution, in units, provided by the HTS screens is presented in figures 12(b) and 12(d) for the rotating coil region. The field solution is reconstructed from the measured multipoles for both the prototypes, at 300 K and 77 K. At cold, the quadrupole field component is dominant in both cases, with a field inhomogeneity qualitatively higher for the first prototype.

5.1.1. Geometric quality analysis.

The field quality measurements of the HALO setup at 77 K without iron bars are used in the PSO algorithm (see section 4.2), obtaining a residual in the penalty function below 0.5 units. The geometric-defect parameters calculated for the HTS screens are given in table 3, for both HTS holders. The first prototype suffers from relevant geometric defects, up to a few millimeters. In the second prototype, the defects related to curvature and rotation are reduced by more than two orders of magnitude.

The geometric-defect parameters determine the shape of the HTS screen in the two prototypes as in figure 13, where geometric defects are graphically magnified by a factor ten. Note that from figure 11, the distortion shown in figure 13 is already apparent. The figure includes also the position of the rotating coil and the horizontal mid-plane. The first prototype is affected by substantial geometric defect, whereas the second prototype is much closer to the reference geometry. A residual deformation of the left screen still persists, leading to a non-perfect parallelism between the tapes.

The self-field contribution from the HTS screens is affected by mechanical tolerances. The worst-case screens in terms of maximum THD factor are numerically determined using the model of the experimental setup. In detail, the PSO algorithm is used for finding the worst-case screen deformation within given constraints, imposed by prescribing the mechanical tolerances as maximum geometric defects in (9). Results are given in figure 14, showing that the THD factor can be kept around 1 unit by applying tolerances of 25 μm. As an example, the same tolerances were used for the manufacturing of the austenitic steel collars of the superconducting coils in the LHC main dipole magnets [42]. For perfectly parallel screens in the thin-shell approximation, the self field error disappears. In practice, due to the finite thickness of the superconducting tapes, the error is negligible but nonzero.

5.2. Prototypes with iron bars

The iron bars are mounted in the magnet aperture, and the magnetic field quality is evaluated. Measurements at 300 K are influenced only by the iron bars, whereas at 77 K the HALO contribution is also included. For the first prototype, the magnetic field quality is given in units as a multipole expansion series in figure 15(a). The iron bars are mounted accordingly to the *medium* error scenario (see table 2), creating 30 units of a_2 and 15 units of a_3, with minor contribution of b_2. The HALO reduces the a_2 a_3 contributions, whereas the b_2, b_3 and

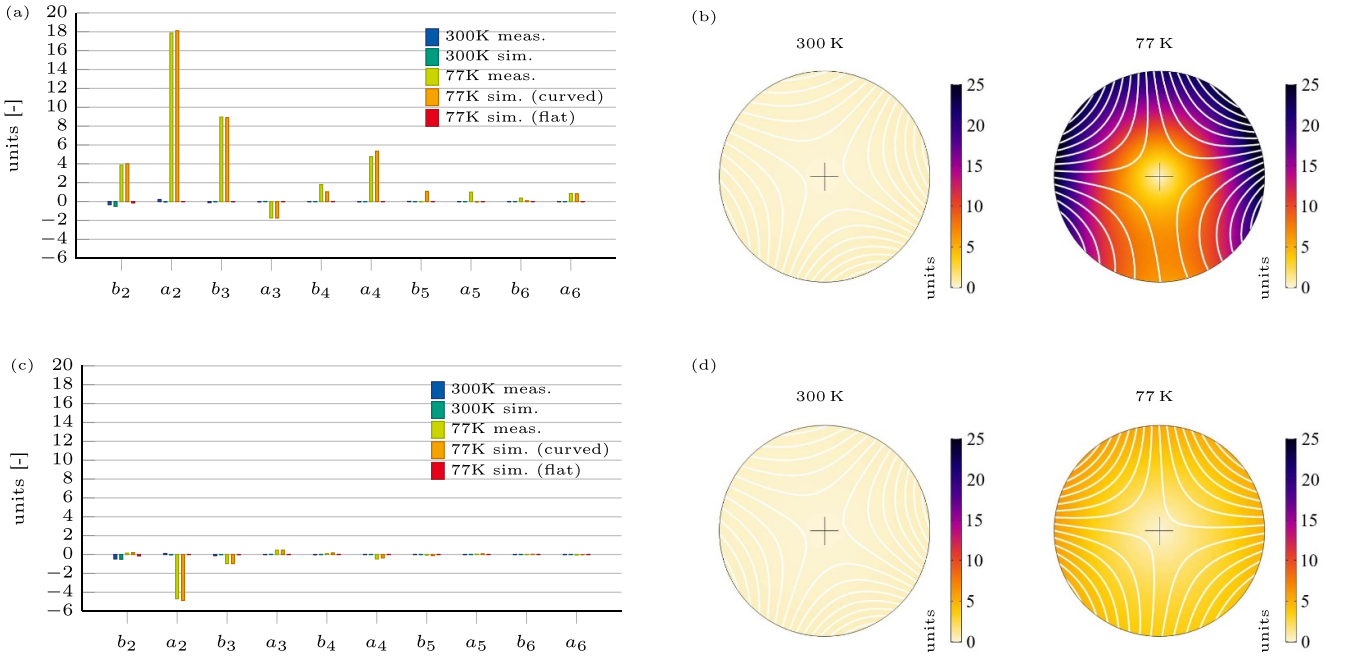

Figure 12. Measured and simulated magnetic field quality, without iron bars. Left: multipole expansion series. Right: magnetic field error seen by the rotating coil. (a) First prototype in dipole field, (b) First prototype in dipole field, (c) Second prototype in dipole field, (d) Second prototype in dipole field.

Table 3. Geometric-defect parameters.

Screen	Error	Unit	1st holder	2nd holder
Left	d_{up}	μm	1200	−1
	d_{dn}	μm	−1900	170
	d_θ	mrad	47	−5
Right	d_{up}	μm	−1000	−75
	d_{dn}	μm	2100	5
	d_θ	mrad	−42	1

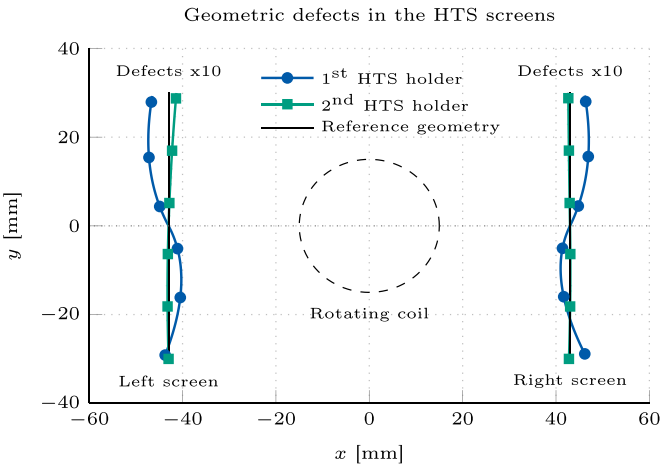

Figure 13. Graphical rendering of the geometric defects in the HTS screens, for both the version of the holder, as well as for an ideal HALO geometry, with perfectly parallel HTS screens. Defects are rendered with a factor ten amplification.

b_4 errors are increased. The increase for b_2, b_3 and b_4 occurs due to the geometric defects in the first HALO prototype (see section 5.1).

For the second prototype, the iron bars are mounted according to all the four scenarios described in table 2. The field error due to the iron bars is characterized for the *low* error scenario (figure 15(c)) by 10 units of a_2, with minor contributions of b_3 and a_3; for the *medium* error scenario (figure 15(e)) by 30 units of a_2 and 15 units of a_3, with minor contribution of b_2; for the *high* error scenario (figure 15(g)) by 70 units of a_2 and 10 units of a_3 with minor contribution from b_2 and a_4. The *check* error scenario (figure 15(i)) introduces an error equal in magnitude to the *medium* error scenario, but with inverted sign for the normal even-order and the skew odd-order multipoles.

Once the HALO is superconducting, the field error is reduced. This observation holds true for for each scenario, and for every field multipole introduced by the iron bars. The reduction factor for the dominant multipoles is between three and four, higher for the components with higher magnitude. The high-order multipoles (>4) are left unperturbed, remaining within the noise floor of the background field. Simulation results show that curved and flat geometries are in qualitative agreement, with the screens working close to ideal conditions.

The net magnetic contribution provided by the HTS screens is shown in figure 15 for the rotating coil region. Results are shown at 300 K and 77 K for the first prototype in a *medium* error scenario, and for the second prototype in the *low*, *medium*, *hard*, and *check* error scenarios. The color scales are consistent only by rows, as the field error in the four scenarios has different magnitude. It is possible to observe for all

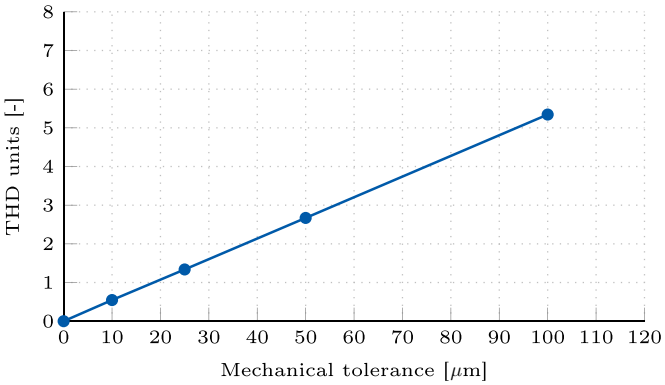

Figure 14. Simulated self-field error, in THD units, as a function of the mechanical tolerance prescribed for the screens. Results are given for the worst-case design within prescribed tolerances.

the scenarios, from the left to the right column, a reduction in the field error and an improvement in the homogeneity of the magnetic field distribution.

5.3. Field-error cancellation

The THD factor, see (13) in the appendix, is calculated for the field-error results in figure 15, for both the first and second prototype. Results are shown in figure 16 for measurements and simulations. The magnetic contribution of the HTS screens causes a reduction of the THD factor for each scenario, for both prototypes. The highest reduction is achieved for the scenario at high field error, where the contribution from the self-field error from the screen is less relevant.

The overall field-cancellation performance of the HTS screens is quantified by means of two efficiency parameters. The geometric efficiency η_g, together with the related geometric quality factor Q_g, measures the performance degradation caused by non ideal screen geometries. It is defined as

$$\eta_g = 1 - \frac{F_d(\boldsymbol{B}_{halo})}{F_d(\boldsymbol{B}_{iron})} = 1 - \frac{1}{Q_g}, \tag{10}$$

where $\boldsymbol{B}_{halo}$ and $\boldsymbol{B}_{iron}$ represent the measured field in the dipole magnet with the HTS screens and the iron bars, respectively. For high efficiency, the self-field error from the screens must be negligible with respect to the overall field error. For perfectly parallel and infinitely thin screens, that is, for $F_d(\boldsymbol{B}_{halo}) \to 0$, the geometrical efficiency $\eta_g \to 1$ and the screens reach the theoretical performance predicted by simulations with flat screens.

The magnetic efficiency η_m, together with the related magnetic quality factor Q_m, measures the overall field quality improvement after the field-error cancellation. It is defined as

$$\eta_m = 1 - \frac{F_d(\boldsymbol{B}_{both})}{F_d(\boldsymbol{B}_{iron})} = 1 - \frac{1}{Q_m}, \tag{11}$$

where $\boldsymbol{B}_{both}$ is the measured magnetic field in the dipole magnet with both the HTS screens and the iron bars. The magnetic efficiency is influenced not only by the geometric defects but also by the width, thickness, and position of the screens. A complete cancellation of the magnetic field error consists in $F_d(\boldsymbol{B}_{both}) \to 0$ and corresponds to the maximum magnetic efficiency $\eta_m \to 1$.

The performance parameters (10) and (11) are reported in table 4 for all the scenarios. The first prototype features $\eta_g = 0.4$, $\eta_m = 0.6$, and $Q_m = 2.4$. A performance increase is observed for second prototype, achieving a η_g up to 0.9 and η_m up to 0.75, delivering a Q_m between 2.9 and 3.8. The field quality is improved by a factor of almost four, for the high field-error scenario. For the scenarios where $Q_g < Q_m$, the HALO self-field error provided a partial compensation of the field error due to the iron bars.

6. Numerical extrapolation

Although the prototype is operated at 77 K and 100 mT, the expected conditions for HTS screens within accelerator magnets are characterized by lower temperatures and higher fields. With respect to the experiment conditions, an increase in the magnetic field and a decrease in the temperature would have opposite effects by respectively decreasing and increasing the critical current of the HTS tapes (see e.g. [43]). For this reason, numerical simulations are used for extrapolating the behavior of the HALO technology to accelerator-like operational conditions.

The HTS screens are assumed to be eventually operated at 4.5 K, in a background dipole field of 10 T which is affected by a b_3 error of ten units. The model is shown in figure 17, where the magnetic field is imposed by a boundary source. The magnetic field and the field-error components are chosen to qualitatively reproduce a field-scenario within the LHC [5]. Simulations retain the geometric setup of the screens and the reference radius from the experiment, with the magnet aperture equal to $3/2$ of the reference radius. The screens are positioned with a horizontal displacement of 2 mm with respect to the magnet aperture. The gap accounts for the structural elements such as the beam screen and the surrounding steel pipe [5].

The b_3 field component has a negligible influence on the orientation of the magnetic field. As a consequence, the magnetic field lines are assumed to be aligned with the HTS screens, achieving a higher critical current I_c in the screens due to the anisotropic behavior of HTS tapes. In the following, a critical current per unit of length $I_c = 250\ \mathrm{A\,mm^{-1}}$ is assumed, consistently with the measurements available for commercial tapes in [43] and [44]. It was verified that the paramagnetic behavior of the Hastelloy substrate at low temperatures [45] provides a negligible contribution to field quality results for a conservative relative permeability $\mu_r = 1.005$, therefore this phenomenon is neglected.

6.1. HTS screens geometry

Moving from the screen geometry used in the prototype, the tapes per layer are increased from 5 to 8 (4 to 7 for the odd-order layers), up to 100 mm wide screens, and the number of layers is increased from 4 to 16. It is worth noting that while the

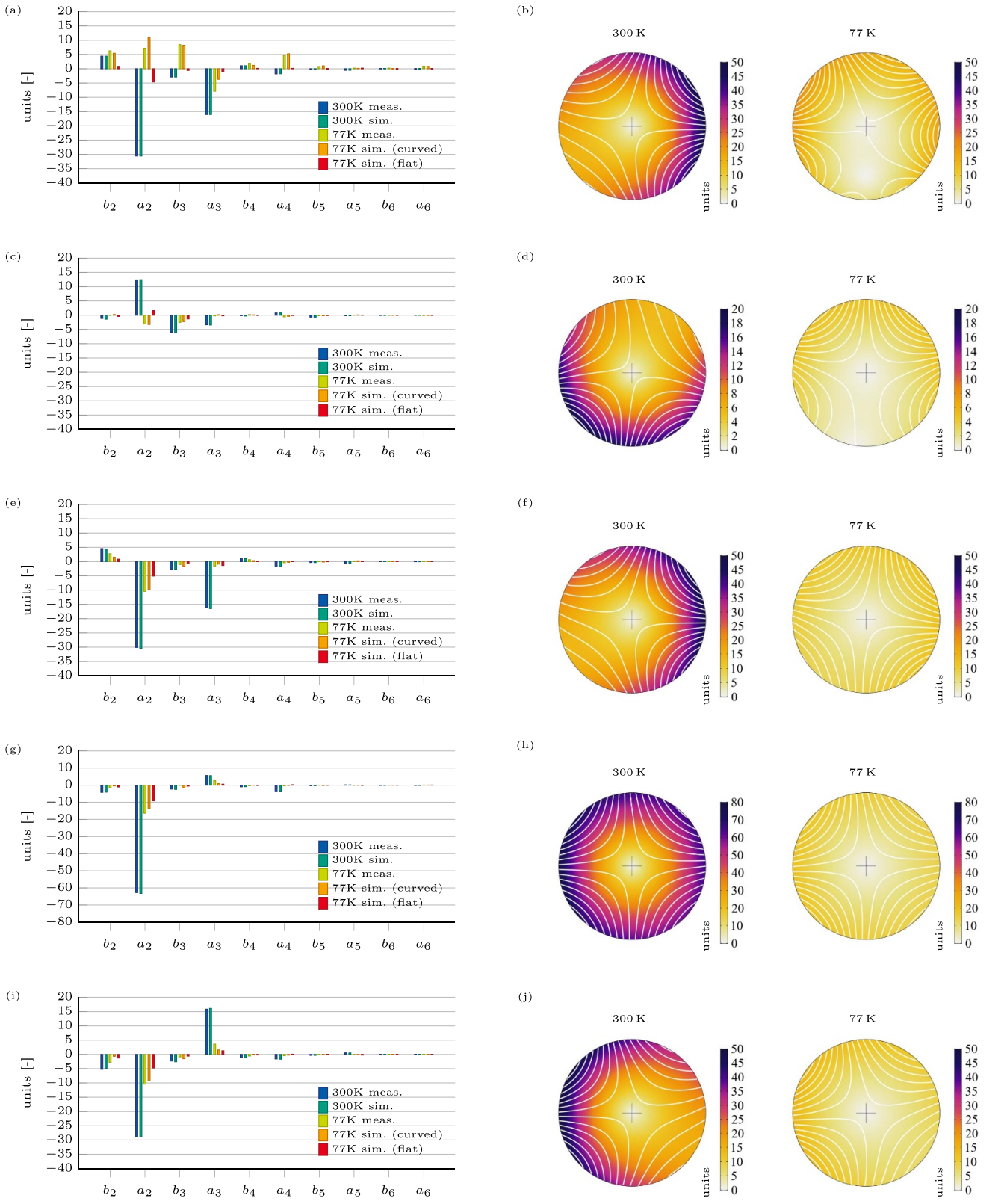

Figure 15. Measured and simulated magnetic field quality, without iron bars. Left: multipole expansion series. Right: magnetic field error seen by the rotating coil. (a) First prototype, medium field error, (b) First prototype, medium field error, (c) Second prototype, low field error, (d) Second prototype, low field error, (e) Second prototype, medium field error, (f) Second prototype, medium field error, (g) Second prototype, high field error, (h) Second prototype, high field error, (i) Second prototype, check field error, (j) Second prototype, high field error.

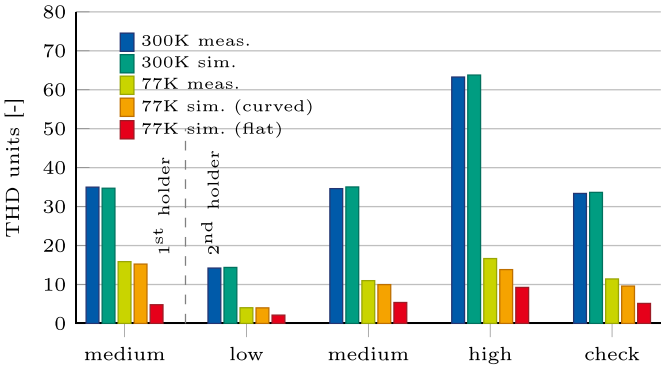

Figure 16. Measured and simulated magnetic field quality, given in units as a THD factor. Results are shown for four different positions of the iron bars. The field error is shown for both the iron bars alone, and with the HALO. Simulation results are also shown for HTS screens with flat geometry.

Table 4. HALO performance results.

No.	Holder	Field error	η_g	η_m	Q_g	Q_m
1	1st	Medium	0.40	0.58	1.7	2.4
2	2nd	Low	0.65	0.72	2.8	3.5
3	2nd	Medium	0.86	0.68	6.9	3.1
4	2nd	High	0.92	0.74	12.6	3.8
5	2nd	Check	0.85	0.66	6.7	2.9

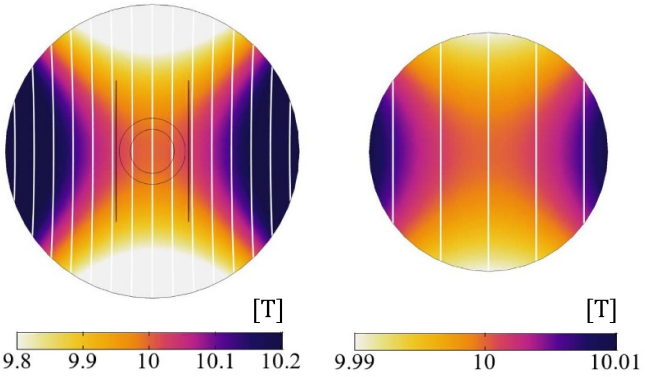

Figure 17. Case study for numerical extrapolation. Left: dipole magnetic field of 10 T, affected by 10 units of b_3. The reference circumference and the magnet aperture are shown in the center. Right: magnetic field inside the reference circumference.

magnet coil design and the clearance of the magnet aperture may pose geometric limits to the screen width, increasing the number of layers shall be eased by the negligible thickness of the tapes.

The magnetic field is linearly increased from zero up to 10 T within 10 s, then it is kept constant. The magnetic field quality is evaluated 100 s after steady state operations. The results, shown in figure 18, are given in terms of the THD factor as a function of the number of tapes per layer, and parametrized with the number of layers in the HTS screens. It is shown that the magnetic field error is reduced below one unit. If a field

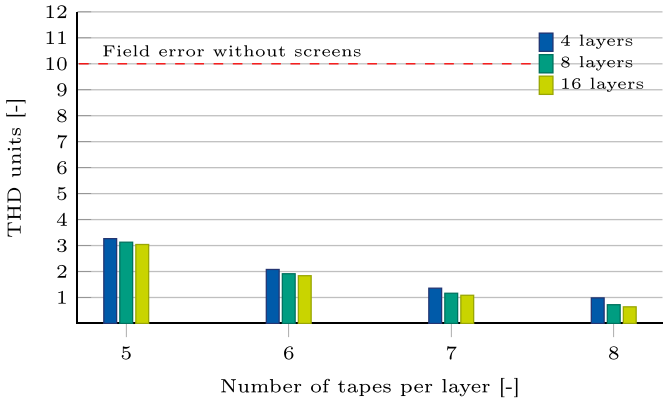

Figure 18. Simulated magnetic field quality. Results are given in units as a THD factor, as a function of the number of tapes per layer, and parametrized with the number of layers in the HTS screens.

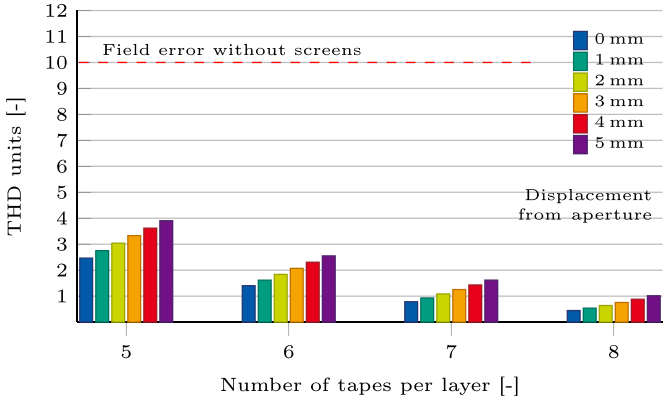

Figure 19. Simulated magnetic field quality for screens of 16 layers. Results are given in units as a THD factor, as a function of the number of tapes per layer, and parametrized with the horizontal displacement of the HTS screens with respect to the magnet aperture.

quality constraint is prescribed, the screen design can be scaled up to match the requirements.

The field-error cancellation is more effective for superconducting screens closer to the magnet aperture. This is shown in figure 19, where the THD factor is calculated for screens of 16 layers as a function of the number of tapes per layer, and parametrized with the distance between the screens and the magnet aperture. For the shortest screen made of 5 tapes, an increase of about 0.3 units per millimeter is found, whereas for the longest screen made of 8 tapes an increase of about 0.1 units per millimter is obtained. For this case, the sensitivity of the screen to the horizontal offset with respect to the magnet aperture is weaker for longer screens.

6.2. Screening currents drift

The magnetic field is linearly increased from zero up to 10 T within 10 s, then it is kept constant. Subsequently, the dynamics of the HTS screens is simulated for up to 100 h of stable operations. In this way, the drift of the screening currents is

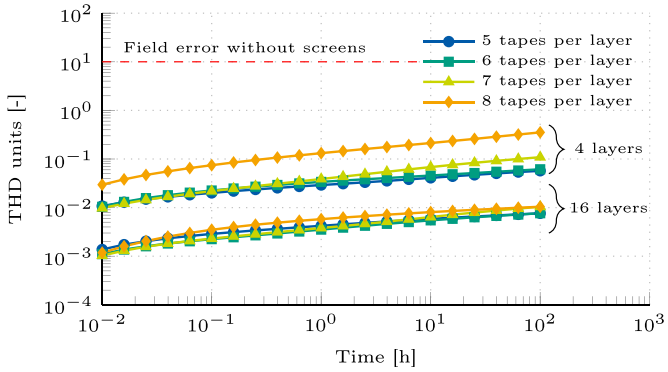

Figure 20. Simulated drift of the THD factor, in units, as a function of time. Results are shown for 100 h of stable operations, and are parametrized by both the number of tapes per layer, and the number of layers.

simulated in steady-state field conditions. The drift is calculated as the increase of the THD factor with respect to the value at the end of the field ramp. Results are shown in figure 20 in terms of drift of the THD factor as a function of time. The curves are parametrized by both the number of tapes per layer, and the number of layers. The increase of the THD factor is expected to remain below 0.01 units within 100 h for the 16-layers configuration. If a constraint is prescribed to the drift of the magnetic field, the screen design can be scaled up to match the requirements.

7. Discussion

The measurements shown in figure 15 show in every scenario a relevant reduction of the field error, after the HALO has transitioned to the superconducting state. The cancellation effect is given by the magnetic contribution of screening currents induced in the HTS tapes.

The cancellation occurs in all the multipole components, contributing to the homogenization of the magnetic field in the magnet aperture, as shown in figure 15. The THD factor is reduced by a factor of three to four (see figure 16), depending on the field-error scenario. The field-error cancellation provided by HALO brings a net improvement of the magnetic field quality. Therefore, the proof of concept can be considered successful.

The two prototypes reached about 70% and 90% of the field-error cancellation predicted by simulations assuming flat screens. The discrepancy is caused by geometric deformations of the HTS screens due to mechanical tolerances which affected the manufacturing of the prototypes. Such deformations have a detrimental influence on the field quality by introducing a self-field error which poses an upper limit to the HALO performance. The self-field error delivers a constant field contribution whose relevance decreases as the overall field error increases.

In this work, the THD factor due to the self-field error was reduced to five units. It is expected that such error can be further reduced by suitable design choices, sufficiently tight mechanical tolerances and a precise manufacturing process. In detail, rigid HTS holders are recommended for the mechanical support of the tapes, for example rectangular blocks can be accurately machined such that their opposite faces provide the geometric reference for dipole screens.

Numerical simulations for flat screens are found in qualitative agreement with measurements, although they overestimate the HALO performance. Geometric deformations were identified in the first HTS holder prototype by means of a visual inspection, and were integrated in the model by means curved screens. Geometric defects were quantified by means of an optimization algorithm, leading to simulations in quantitative agreement with measurements. Optimization results shall be used carefully, since over-fitting is a risk, for example of the superconducting properties of the tapes. However, the geometric defects for the two prototypes are determined only once and in the absence of iron. With the subsequent addition of iron, and in spite of the absence of 're-fitting' for geometric defects, the measured and simulated results in figure 15 show a high degree of consistency, which is a strong indication of the excellent predictive value of the simulation model.

The HTS screens are simulated at 4.5 K and in 10 T dipole background field, for working conditions typical of accelerator magnets. The field-error cancellation is still effective as long as the equivalent critical current density of the screens is increased accordingly, that is, by increasing the number of layers and decreasing the operational temperature. Numerical results show also that the field-error cancellation can be improved by increasing of the width and the number of layers of the HTS screens. The THD factor is reduced below one unit, leading to a nearly perfect cancellation of the field error. The decay of the screening currents over time, and the consequent degradation of the field quality, is expected to remain within 0.1 units over 10 h, being negligible in comparison with the operating time of accelerator circuits [5]. The persistency of the screening currents is the cornerstone of the overall HALO technology. For this reason, the screening currents decay rate must cope with the field quality requirements in the target application. The field drift can be kept within specifications by choosing in the design phase appropriate features for HALO, such as the critical current of the tapes and number of layers in the screens.

In an accelerator magnet, the HTS screens must be centered as close as possible around the beam vacuum chamber. The HALO technology is expected to provide the maximal benefit to magnets made of ReBCO tapes, as at low current the field quality is those magnets is expected to be heavily degraded by persistent magnetization phenomena. The maximum field error that can be canceled is determined by the equivalent critical current of the HTS screens. This design parameter can be increased either by adding layers to the screens, or by decreasing the operational temperature. In order to integrate HALO in accelerator magnets, the combination of both the strategies is envisioned, as the magnetic fields are expected to be up to two orders of magnitude higher than in the experimental setup used for the proof of concept. For this reason, an operational temperature below 20 K is recommended.

8. Conclusions and outlook

This paper presents the proof of concept for HALO, a technology for field-error cancellation based on ReBCO tapes composing passive and self-regulating HTS screens. The working principle relies on the persistent magnetization from screening currents for shaping the magnetic field in a given region of space, for example the aperture of accelerator magnets. By aligning the screens to the desired field shape, this technology allows for a selective field-error cancellation for both the dynamic and static contribution to the error.

In the analysis of the results on the first prototype it was found that geometric defects in this prototype have a detrimental effect on the measured field quality. The lessons learned from the first prototype were applied to the second prototype, and the observed geometric distortion was found to be substantially better. The field quality is measured in four field-error configurations obtained with different positions for the iron bars. It was found that the HALO prototype provides a significant reduction of the THD factor associated to the field error, up to a factor four, reaching up to 90% of the performance expected by numerical simulations.

Measurements are compared with simulations. The analysis is carried out under magnetoquasistatic assumptions, using time-domain simulations based on a coupled $\boldsymbol{A}$-$\boldsymbol{H}$ formulation implemented in a 2D FEM model. Simulations provide the HALO theoretical performance in case of perfectly parallel HTS screens, and quantify the geometric defects for the screens in the experimental setup, achieving quantitative agreement with measurements. Numerical extrapolation shows that a complete error cancellation may be achieved by increasing the width and the thickness of the screens, for operational conditions compatible with accelerator magnets. At the same time, the field-quality drift due to the persistent currents decay can be kept within specifications by a suitable choice of design parameters.

The HTS screens are applicable regardless of the technology used for the magnet, as long as they are kept in superconducting state, and might be of use for applications beyond accelerators where stringent field quality requirements need to be satisfied.

Acknowledgments

This work has been sponsored by the Wolfgang Gentner Programme of the German Federal Ministry of Education and Research (Grant No. 05E15CHA), and by Graduate School CE within the Centre for Computational Engineering at the Technische Universität Darmstadt.

The authors would like to thank A Ballarino and S Hopkins for the procurement of the HTS tape, M Timmins for the support with the technical drawings, P Frichot for the procurement of the mechanical parts, M Liebsch, S Richter and T Nes for useful discussions about the design of the experimental setup, and L Fiscarelli for the support with measurements. The authors acknowledge the fruitful collaboration between CERN and the Technische Universität Darmstadt, within the framework of the STEAM collaboration project [46].

Appendix. Magnetic field quality

In accelerator magnets, the magnetic field quality is traditionally defined as a set of Fourier coefficients known as multipoles. These field coefficients are given by the solution of the Laplace equation $\Delta \boldsymbol{A} = 0$ in the magnet aperture, for the cross sectional plane of the magnet aperture. The multipole expansion series [6] is calculated at the reference radius r_0, usually chosen as 2/3 of the magnet aperture. By decomposing the magnetic field $\boldsymbol{B}$ by means of complex notation as $\boldsymbol{B} = B_\mathrm{y} + iB_\mathrm{x}$, the series reads

$$\boldsymbol{B} = \frac{B_1}{1\times 10^4}\sum_{k=1}^{\infty}(b_k + ia_k)\left(\frac{x+iy}{r_0}\right)^{k-1}, \qquad (12)$$

where B_1 is the dipole field component, k is the order of the eigensolution generated by ideal magnet geometries, and b_k and a_k are the $2k$-pole normal and skew coefficients, given in units (1×10^{-4} of the main field). Therefore, in dipole fields the magnetic field error is quantified by the magnitude of the $k \geqslant 2$ multipole coefficients.

The total harmonic distortion (THD) factor F_d is a scalar quantity defined for $r = r_0$ as

$$F_\mathrm{d}(\boldsymbol{B}) = \sqrt{\sum_{k=2}^{\infty}(a_k^2 + b_k^2)}. \qquad (13)$$

In this paper, the calculation of F_d is done up to the dodecapole components ($k = 6$), consistently with (9). The numerical evaluation of the field quality is obtained by sampling the magnetic field solution along the reference circumference over 4096 points homogeneously distributed. Subsequently, the multipole coefficients are calculated by means of a fast Fourier transform algorithm applied to the radial field component [6].

ORCID iDs

L Bortot https://orcid.org/0000-0003-0409-7287
M Mentink https://orcid.org/0000-0001-9769-0578
J Van Nugteren https://orcid.org/0000-0001-8072-7725

References

[1] FCC collaboration 2019 FCC-hh: the Hadron collider: future circular collider conceptual design report volume 3 *Eur. Phys. J. Spec. Top.* **228** 755–1107
[2] Van Nugteren J *et al* 2018 Toward REBCO 20 T+ dipoles for accelerators *IEEE Trans. Appl. Supercond.* **28** 1–9
[3] Golovashkin A, Ivanenko O, Kudasov Y B, Mitsen K, Pavlovsky A, Platonov V and Tatsenko O 1991 Low temperature direct measurements of Hc2 in HTSC using megagauss magnetic fields *Physica* C **185** 1859–60
[4] Wilson M N 1983 *Superconducting Magnets* (Oxford: Clarendon)
[5] Brüning O *et al* 2004 *LHC Design Report* (European Organization for Nuclear Research)
[6] Russenschuck S 2011 *Field Computation for Accelerator Magnets: Analytical and Numerical Methods for*

Electromagnetic Design and Optimization (New York: Wiley)
[7] Shi J and Yao D 2000 Collective beam-beam effects in hadron colliders *Phys. Rev.* E **62** 1258
[8] Fazilleau P, Borgnolutti F, Dilasser G and Durante M 2018 Screening currents within the EuCARD HTS dipole *IEEE Trans. Appl. Supercond.* **28** 1–5
[9] Noguchi S, Ueda H, Hahn S, Ishiyama A and Iwasa Y 2019 A simple screening current-induced magnetic field estimation method for REBCO pancake coils *Supercond. Sci. Technol.* **32** 045007
[10] Gömöry F, Solovyov M, Šouc J, Navau C, Prat-Camps J and Sanchez A 2012 Experimental realization of a magnetic cloak *Science* **335** 1466–8
[11] Tomków Ł, Ciszek M and Chorowski M 2015 Combined magnetic screen made of bi-2223 bulk cylinder and ybco tape rings—modeling and experiments *J. Appl. Phys.* **117** 043901
[12] Frollo I, Andris P, Krafčík A, Gogola D and Dermek T 2018 Magnetic field homogeneity adjustment for magnetic resonance imaging equipment *IEEE Trans. Magn.* **54** 1–9
[13] Wang T, Xiao S, Liu X and Li Y 2016 A 3.35 T actively shielded superconducting magnet for dynamic nuclear polarization device *IEEE Trans. Appl. Supercond.* **26** 1–4
[14] Tomków Ł, Kulikov E, Kozłowski K and Drobin V 2019 Improvement of the homogeneity of magnetic field by the attenuation of a selected component with an open superconducting shield made of commercial tapes *J. Appl. Phys.* **126** 083903
[15] van Nugteren J, Murtomäki J, Kirby G, De Rijk G, Rossi L, and ten Kate H 2016 Persistent current shim coils for future high field accelerator magnets *Technical Report* No. EDMS 1574002 (CERN, Geneva) (available at: https://edms.cern.ch/ui/#!master/navigator/document?D:1255633525:1255633525:subDocs)
[16] van Nugteren J 2016 High temperature superconductor accelerator magnets PhD Dissertation Twente U., Enschede
[17] Bíró O 1999 Edge element formulations of Eddy current problems *Comput. Methods Appl. Mech. Eng.* **169** 391–405
[18] Brambilla R, Grilli F, Martini L, Bocchi M and Angeli G 2018 A finite-element method framework for modeling rotating machines with superconducting windings *IEEE Trans. Appl. Supercond.* **28** 1–11
[19] Dular J, Geuzaine C and Vanderheyden B 2019 Finite element formulations for systems with high-temperature superconductors *IEEE Trans. Appl. Supercond.* **30** 1–13
[20] Bortot L, Auchmann B, Garcia I C, De Gersem H, Maciejewski M, Mentink M, Schöps S, Van Nugteren J and Verweij A P 2020 A coupled A–H formulation for magneto-thermal transients in high-temperature superconducting magnets *IEEE Trans. Appl. Supercond.* **30** 1–11
[21] Walckiers L 1992 The harmonic-coil method, parts 1 and 2 *CERN Accelerator School: Magnetic Measurement and Alignment (16–20 March 1992)* (CERN) pp 138–65
[22] Jain A K 1992 Harmonic coils *CERN Accelerator School: Measurement and Alignment of Accelerator and Detector Magnets (11–17 April 1992)* (CERN) pp 175–213
[23] Superpower Inc. 2019 (available at: www.superpower-inc.com/) (Accessed 1 July 2021)
[24] Arpaia P, Bottura L, Fiscarelli L and Walckiers L 2012 Performance of a fast digital integrator in on-field magnetic measurements for particle accelerators *Rev. Sci. Instrum.* **83** 024702
[25] Hu D, Ainslie M D, Raine M J, Hampshire D P and Zou J 2016 Modeling and comparison of in-field critical current density anisotropy in high-temperature superconducting (HTS) coated conductors *IEEE Trans. Appl. Supercond.* **26** 1–6
[26] Krähenbühl L and Muller D 1993 Thin layers in electrical engineering-example of shell models in analysing eddy-currents by boundary and finite element methods *IEEE Trans. Magn.* **29** 1450–5
[27] Bossavit A 1988 A rationale for 'edge-elements' in 3-D fields computations *IEEE Trans. Magn.* **24** 74–79
[28] Brambilla R, Grilli F and Martini L 2006 Development of an edge-element model for AC loss computation of high-temperature superconductors *Supercond. Sci. Technol.* **20** 16
[29] Emson C and Simkin J 1983 An optimal method for 3-D Eddy currents *IEEE Trans. Magn.* **19** 2450–2
[30] Alonso Rodríguez A and Valli A 2008 Voltage and current excitation for time-harmonic Eddy-current problems *SIAM J. Appl. Math.* **68** 1477–94
[31] Schöps S *et al* 2013 Winding functions in transient magnetoquasistatic field-circuit coupled simulations *COMPEL - Int. J. Comput. Math. Electr. Electron. Eng.* **32** 2063–83
[32] Ruiz-Alonso D, Coombs T A and Campbell A M 2004 Numerical analysis of high-temperature superconductors with the critical-state model *IEEE Trans. Appl. Supercond.* **14** 2053–63
[33] Pentella M 2021 Magnetic characterization of pure iron for the halo project *Technical Report* No. EDMS 2476554 (CERN, Geneva) (available at: https://edms.cern.ch/ui/#!master/navigator/document?D:100765686:100765686:approvalAndComments)
[34] Wu M-K, Ashburn J R, Torng C, Hor P H, Meng R L, Gao L, Huang Z J, Wang Y and Chu A 1987 Superconductivity at 93 K in a new mixed-phase Y-Ba-Cu-O compound system at ambient pressure *Phys. Rev. Lett.* **58** 908
[35] Rhyner J 1993 Magnetic properties and AC-losses of superconductors with power law current–voltage characteristics *Physica* C **212** 292–300
[36] Yamafuji K and Kiss T 1997 Current-voltage characteristics near the glass-liquid transition in high-Tc superconductors *Physica* C **290** 9–22
[37] Sirois F, Grilli F and Morandi A 2018 Comparison of constitutive laws for modeling high-temperature superconductors *IEEE Trans. Appl. Supercond.* **29** 1–10
[38] Dew-Hughes D 1988 Model for flux creep in high Tc superconductors *Cryogenics* **28** 674–7
[39] 2018 MATLAB version 9.5.0.944444 (R2018b) (Natick, MA: The Mathworks, Inc.)
[40] Kennedy J and Eberhart R 1995 Particle swarm optimization *Proc. ICNN'95-Int. Conf. on Neural Networks* vol 4 (IEEE) pp 1942–8
[41] COMSOL 2020 COMSOL multiphysics, v. 5.3, [CD-ROM] (Stockholm, Sweden: COMSOL AB)
[42] Bellesia B, Bertinelli F, Santoni C and Todesco E 2006 Dependence of magnetic field quality on collar supplier and dimensions in the main LHC dipole *IEEE Trans. Appl. Supercond.* **16** 196–9
[43] Senatore C, Barth C, Bonura M, Kulich M and Mondonico G 2015 Field and temperature scaling of the critical current density in commercial REBCO coated conductors *Supercond. Sci. Technol.* **29** 014002
[44] Benkel T, Miyoshi Y, Escamez G, Gonzales D, Chaud X, Badel A and Tixador P 2016 REBCO performance at high field with low incident angle and preliminary tests for a 10-T insert *IEEE Trans. Appl. Supercond.* **26** 1–5
[45] Lu J, Choi E and Zhou H 2008 Physical properties of Hastelloy® c-276™ at cryogenic temperatures *J. Appl. Phys.* **103** 064908
[46] STEAM 2019 Simulation of transient effects in accelerator magnets (available at: https://cern.ch/steam) (Accessed 1 May 2020)